Nanoscale Research Letters

NANO EXPRESS Open Access

Reduced Energy Barrier for Li^+ Transport Across Grain Boundaries with Amorphous Domains in LLZO Thin Films

Yanlin Zhu[1], Shuai Wu[1], Yilan Pan[1], Xiaokun Zhang[1*], Zongkai Yan[1*] and Yong Xiang[1,2*]

Abstract

The high-resistive grain boundaries are the bottleneck for Li^+ transport in $Li_7La_3Zr_2O_{12}$ (LLZO) solid electrolytes. Herein, high-conductive LLZO thin films with cubic phase and amorphous domains between crystalline grains are prepared, via annealing the repetitive LLZO/Li_2CO_3/Ga_2O_3 multi-nanolayers at 600 °C for 2 h. The amorphous domains may provide additional vacant sites for Li^+, and thus relax the accumulation of Li^+ at grain boundaries. The significantly improved ionic conductivity across grain boundaries demonstrates that the high energy barrier for Li^+ migration caused by space charge layer is effectively reduced. Benefiting from the Li^+ transport paths with low energy barriers, the presented LLZO thin film exhibits a cutting-edge value of ionic conductivity as high as 6.36×10^{-4} S/cm, which is promising for applications in thin film lithium batteries.

Keywords: Solid electrolytes, LLZO, Thin film, Energy barrier, Ionic conductivity

Introduction

As the rise of 5G mobile telecommunication network, the power consumption of mobile terminals is expected to significantly increase [1–3]. Thin film lithium batteries (TFLBs) with high energy density, long cycle life, and excellent safety hold great promise for the integrated power sources in the intelligent terminals, such as smart cards [4]. To date, most of the workable TFLBs are based on LiPON solid electrolyte [5]. But the low ionic conductivity of LiPON limits the performance of TFLBs. Garnet $Li_7La_3Zr_2O_{12}$ (LLZO) is another promising alternative, due to its high ionic conductivity, wide electrochemical window, and stability against to Li metal anodes [6–10]. However, it remains a challenge to fabricate LLZO thin films with high ionic conductivity [11, 12].

It is well-known that the energetically favorable paths for Li^+ transport are one of the keys to achieving high ionic conductivity in solids [13, 14]. For the case of polycrystalline LLZO thin films, there are two energy barriers that determine the Li^+ conducting performance. One is related to Li^+ transport within a grain. The lattice sites possibly occupied by Li^+ are energetically nonequivalent, and thus Li^+ must get over an energy barrier (EB_g) when it hops between these sites [15–18]. The other one is related to Li^+ transport across the grain boundaries (GBs) [19, 20]. The lattice defects at GBs would cause the accumulation of Li^+. A space charge layer would form because the unoccupied possible sites for Li^+ around GBs are depleted (orange line in Fig. 1a). The space charge effect results in a high migration energy barrier (EB_{gb}, red line in Fig. 1a) [21]. Typically, EB_{gb} (~ 0.7 eV) is much higher than EB_g (~ 0.3 eV) for the case of LLZO [20].

It has been reported that the possible sites for Li^+ occupation in the LLZO with cubic phase, which are tetrahedral 24d site (Li1) and distorted octahedral 96 h site (Li2), are close to energetically equivalent [16, 22, 23]. Therefore, it is generally believed that the EB_g in the cubic LLZO is moderate (~ 0.3 eV). Although the cubic phase of LLZO is metastable at room temperature (RT),

* Correspondence: zxk@uestc.edu.cn; yanzongkai@uestc.edu.cn; xyg@uestc.edu.cn
[1]School of Materials and Energy, University of Electronic Science and Technology of China, Chengdu 611731, Sichuan, China
Full list of author information is available at the end of the article

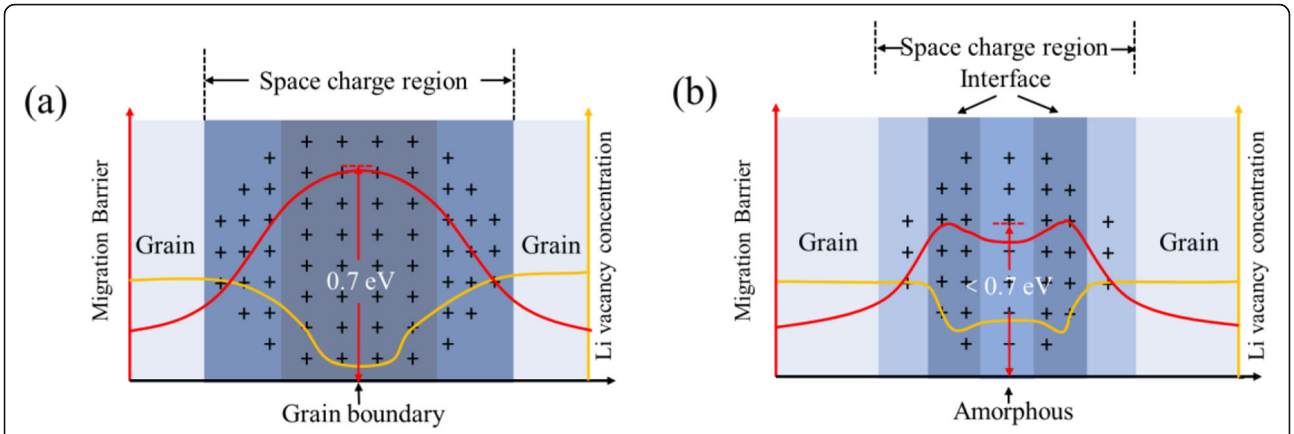

Fig. 1 Illustration of the migration barrier and Li vacancy concentration at the conventional grain boundary (**a**), and the grain boundary with amorphous domains (**b**)

the strategies to stabilize it through the doping of high valence cations, such as Al^{3+}, Ga^{3+}, and Ta^{5+}, have been well developed [24–33]. Lobe et al. reported Al-doped LLZO thin films with ionic conductivity of 1.2×10^{-4} S/cm and activation energy of 0.47 eV [34]. It is generally believed that the high concentration of Li^+ in the crystal lattice may further help to lower EB_g [11, 13]. LLZO thin films with activation energy of 0.38 ± 0.02 eV have been prepared by introducing extra Li_2O during thin film deposition [12, 35]. Li_2O effectively compensated the lithium loss during sputtering-deposition. On the other hand, the strategy to address the conduction issues derived from high EB_{gb} is few, although it is well-known the high-resistive GBs is the bottleneck for Li^+ transport in LLZO [14, 21].

In this work, we demonstrate a LLZO thin film with amorphous domains between crystalline grains. The amorphous domains could provide extra Li^+ vacancies [21, 36–38] and a lower migration barrier (~ 0.6 eV) [36] at GBs (Fig. 1b), which would weaken the space charge effect and lower EB_{gb} (< 0.7 eV) [21, 38]. The presented LLZO thin film is prepared via repeatedly depositing the sequentially stacked nanolayers of LLZO, Li_2CO_3, and Ga_2O_3, and the following annealing (Fig. 2). The ultrathin thicknesses of each layer facilitate the interdiffusion in the multilayered structure, in turn enable Ga_2O_3 to help to stabilize the cubic phase of LLZO, and Li_2CO_3 to compensate the Li loss during deposition and annealing. Through carefully tuning the temperature of annealing, the LLZO thin film with the desired cubic phase and amorphous domains between grains was obtained. The electrochemical impedance measurement suggests the presented LLZO thin film solid electrolyte achieves a high ionic conductivity of 6.36×10^{-4} S/cm.

Methods

Fabrication of Ga-LLZO Thin Film Solid-State Electrolyte

The ultrathin layers of LLZO, Li_2CO_3, and Ga_2O_3 were sequentially deposited by radio frequency magnetron sputtering on polished MgO (100) substrates in pure Ar atmosphere. A multilayered thin film with the thickness of ~ 1500 nm (± 10%) was obtained by repeatedly deposited the triple-layered unit for 80 cycles (Figure S1). The targets of $Li_7La_3Zr_2O_{12}$ (99%), Li_2CO_3(99%), and

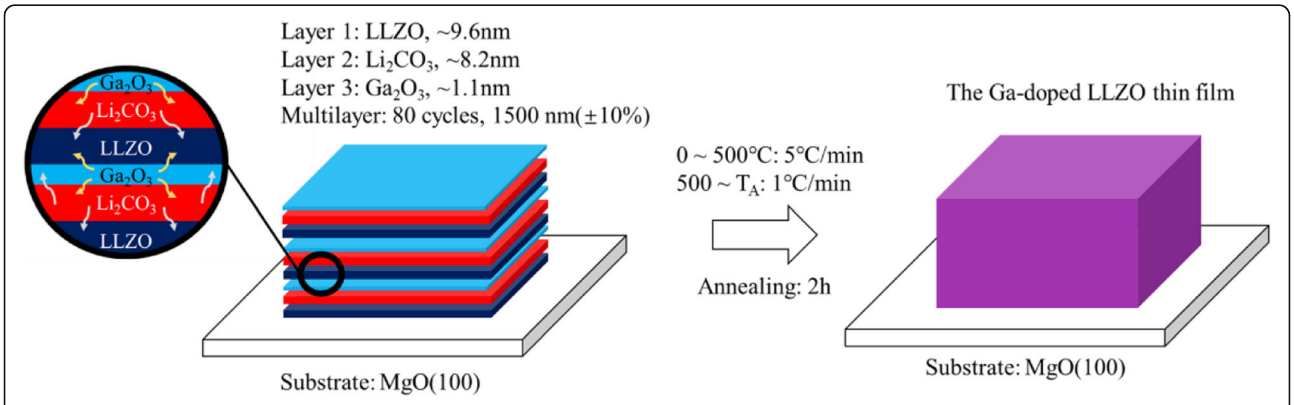

Fig. 2 Schematics of fabrication procedures of the presented LLZO thin films

Ga_2O_3(99.9%) mounted on 190 mm × 55 mm Cu backing plates are provided by Zhongnuo New Materials Manufacturing Co., China. The LLZO target used here is with desired cubic phase (Figure S2) and its density is 5.35 g/cm^3. The pressure for the deposition is 1 Pa. The power density for LLZO deposition was 2.38 W cm^{-2}, and 1.90 W cm^{-2} for Li_2CO_3 and Ga_2O_3. The as-deposited multilayered thin films were further annealed in pure oxygen (99.99%) for 2 h at 600 °C, 700 °C, and 800 °C, respectively.

Characterization

The thickness of each single layer of LLZO, Li_2CO_3, and Ga_2O_3 was determined by a step profiler (see details in Note S1 and Table S1). The crystallographic structure of the thin film was determined using X-ray diffraction (XRD), with Cu-Kα source and 2θ in the range from 10 to 60°. The chemical composition was characterized using time-of-flight secondary ion mass spectrometry (TOF-SIMS) and high-resolution transmission electron microscopy (HRTEM) equipped with an energy dispersive X-ray spectroscopy (EDX) detector. The ionic conductivity was determined in an in-plane test configuration at room temperature (25 °C), via measuring electrochemical impendence spectroscopy (EIS) with the applied frequency ranged from 3 × 10^6 to 1 Hz with a constant 30 mV AC amplitude. The aluminum contacts on the top of LLZO thin films were fabricated using direct current magnetron sputtering. The data of EIS was processed using the Zview software.

Results and Discussion

The LLZO thin film samples and their process parameters were summarized in Table 1. Sample #800-1 without Li-supplementary and Ga-doping exhibits a Li-deficient phase of $La_2Zr_2O_7$ (LZO) after annealing at 800 °C for 2 h (Fig. 3a). After introducing Ga_2O_3 and Li_2CO_3, the diffraction peaks belonging to the cubic phase of LLZO are observed in the XRD pattern of #800-2 (Fig. 3b). This suggests that Ga dopant and extra Li would be favorable for the formation and/or stabilization of the desired cubic phase of LLZO. However, a strong diffraction peak at 28.2° indexed to LZO remains in the XRD pattern of #800-2. As the annealing temperature decreases to 700 °C, the intensity of the diffraction peak at 28.2° declined appreciably (Fig. 3c). These observations indicate that the high temperature annealing may lead to a severe Li loss even though extra Li is introduced. Through further reducing the annealing temperature to 600 °C, the thin film with a major phase of cubic LLZO and a negligible diffraction peak of LZO were obtained (Fig. 3d). Our observations are consistent with previous literature [11, 12], which report that the formation of the cubic phase in Ga-doped LLZO thin films is triggered at 600 °C, and LZO may form within 700 to 800 °C.

Table 1 Samples of LLZO thin film solid electrolyte and their preparation parameters

Samples	Annealing temperature (°C)	Gallium doping	Extra lithium
#800-1	800	×	×
#800-2	800	√	√
#700-1	700	√	√
#600-1	600	√	√

Meanwhile, there are no diffraction peaks of Li_2CO_3 or Ga_2O_3 observed in the XRD patterns (Fig. 3). In addition, the compositional depth profile of #600-1 obtained using TOF-SIMS shows that the signal of CO_3^{2-} is very low through the whole thin film (orange line in Fig. 4). And the competent content of Li in #600-1 is demonstrated by the high intensity of the recorded counts of $^6Li^+$ (red line in Fig. 4). Thus, Li_2CO_3 in the multilayered thin film should have completely decomposed after annealing at 600 °C for 2 h, and effectively compensated the Li loss during thin film deposition and heat treatment. In addition, the undesired reaction between LLZO and CO_2, which may form a low-conductive layer of Li_2CO_3, should be effectively prevented by the annealing atmosphere of pure oxygen. This inference is consistent with the measured high ionic conductivity of #600-1 (see below).

TOF-SIMS characterization also reveals the even distribution of $^6Li^+$, La^{3+}, Zr^{4+}, and Ga^{3+} throughout the thin film #600-1 (Fig. 4). Typically, the interdiffusion of the precursors should be the speed control step in solid-state reactions. Huang et al. reported that the interdiffusion distance of the Ga_2O_3 and LLZO precursor layers was about 10–20 nm during an annealing process at 700 to 900 °C for 2 h. Thus, the thickness of each precursor layer in this study was set to be less than 10 nm. The multilayered structure based on the nanolayers of LLZO, Li_2CO_3, and Ga_2O_3 fabricated here, facilitates the homogenous mixing of the precursors via reducing their necessary diffusion length significantly. The uneven distribution of doped element observed in the LLZO thin films derived from the thicker precursor layers [11] are not observed here. An enrichment of Li in the interphase layer between the deposited thin film and MgO substrate can be observed. This should ascribe to the diffusion of Li^+ into MgO lattice [34].

Briefly, the multilayers of LLZO/Li_2CO_3/Ga_2O_3 are well-mixed and reacted, benefiting from the sufficient interdiffusion among these ultrathin layers. Moreover, the reaction kinetics in the multilayered thin films with doped Ga and extra Li are optimized at 600 °C, for the sake of trying to prepare the cubic phase of LLZO with a low EB_g.

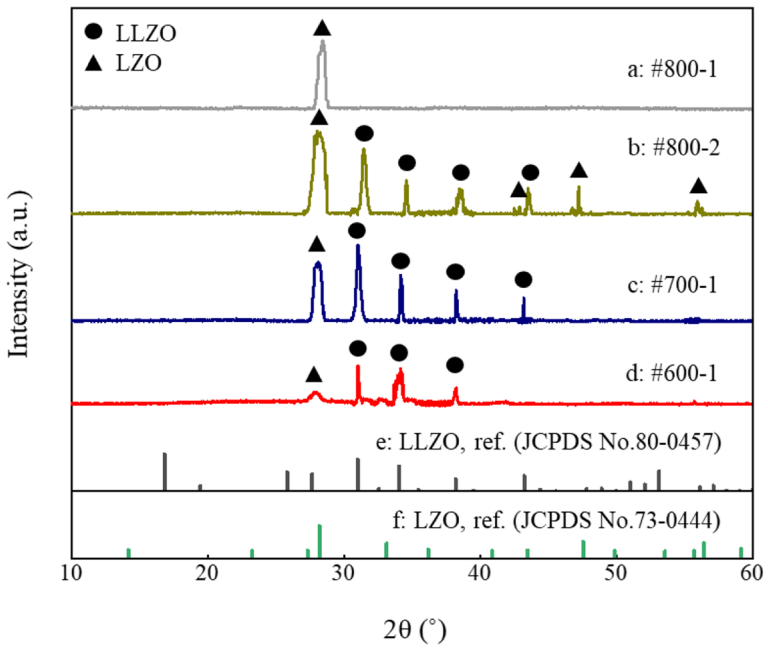

Fig. 3 XRD patterns of #800-1 (**a**), #800-2 (**b**), 700-1 (**c**), and #600-1 (**d**), and the standard diffraction patterns for cubic LLZO (**e**) and LZO (**f**)

As mentioned above, the Li^+ conducting performance of LLZO is notably influenced by the structures at GBs (Fig. 1). The microstructure of #600-1 is carefully characterized using HRTEM. The crossed structure, which is a typical indicator of the reactions between LLZO and H_2O or CO_2 [35], can be observed in the HRTEM images. However, the XRD pattern and TOF-SIMS depth profile of #600-1 suggest that the as-prepared LLZO thin films prevent from reacting with H_2O or CO_2. Thus, it is reasonable to ascribe the formation of crossed structure to the exposure of LLZO thin films to air during the preparation of testing samples. Remarkably, amorphous domains between crystalline grains are observed (Fig. 5a, b). It indicates that #600-1 LLZO thin film should be not fully crystallized after annealing, which is consistent with the relative large full width at half maximum (FWHM) observed in the XRD pattern of #600-1 (Fig. 3d). EDX mapping reveals the uniform distribution

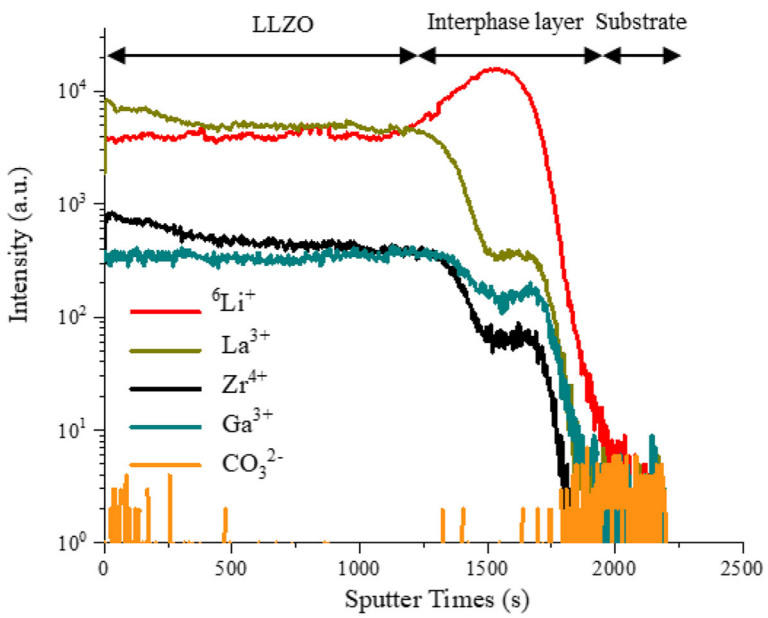

Fig. 4 TOF-SIMS depth profiles of #600-1: $^6Li^+$ (red), La^{3+} (green), Zr^{4+} (black), Ga^{3+} (indigo), CO_3^{2-} (orange)

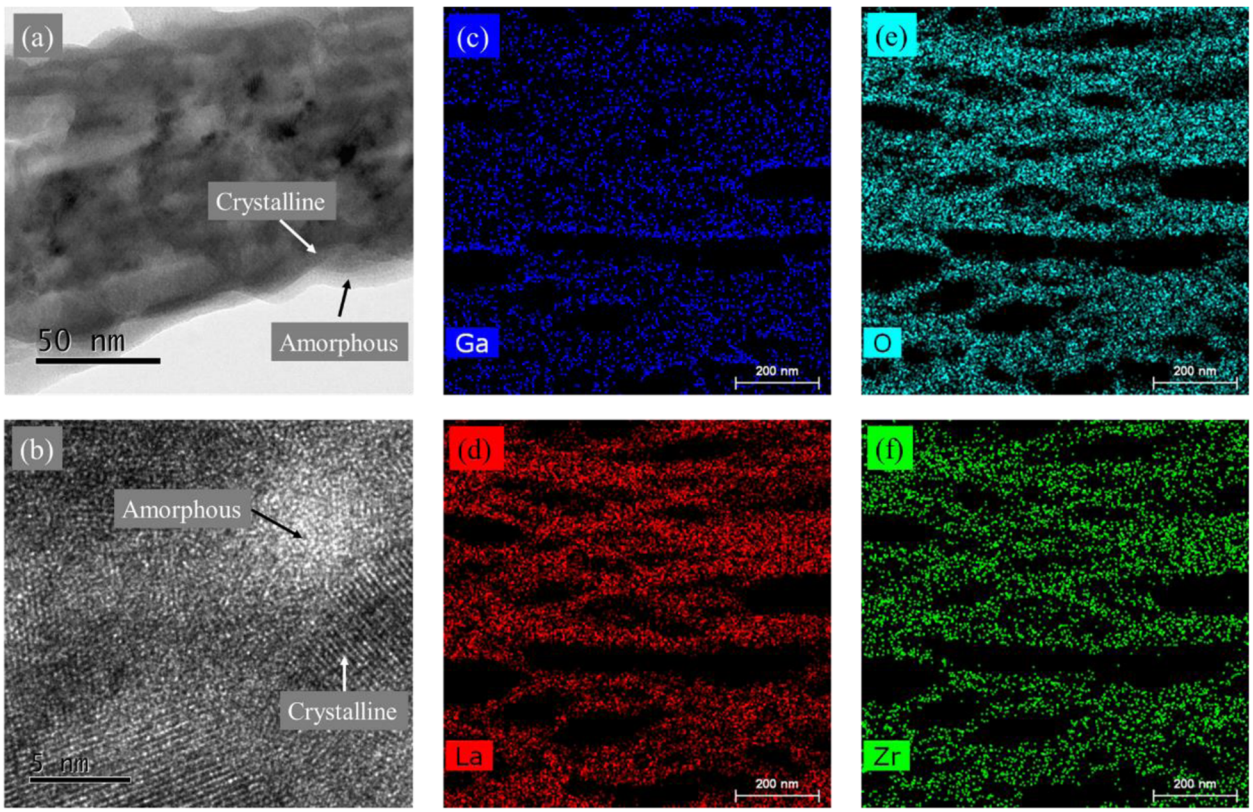

Fig. 5 HRTEM images (**a**, **b**) and elemental mapping (**c** for Ga, **d** for La, **e** for O, **f** for Zr) of LLZO thin film #600-1

of Ga, La, O, and Zr over the crystalline grains and amorphous domains (Fig. 5c–f). Therefore, we propose that the amorphous domains are composed of glassy Li-Ga-La-Zr-O oxides. It has been known that amorphous LLZO is a Li^+ conductor. Its typical ionic conductivity and activation energy are 1×10^{-6} S/cm and ~ 0.6 eV, respectively [36]. The Li^+-conductive amorphous domains would improve the physical contact between crystalline grains, and thus, the paths for Li^+ transport in the thin films are with a better continuity [20]. More importantly, the amorphous domains between the grains are potential to provide additional vacant sites for Li^+ [21, 36–38]. The electrostatic repulsion between Li^+ would be reduced, compared with the conventional LLZO GBs in which the possible sites for Li^+ occupation are depleted [19, 20]. In other words, the amorphous domains may diminish the cacoethic space charge effects and lower the EB_{gb} for Li^+ transport across GBs (Fig. 1b). Consequently, it is reasonable to expect a reduced grain boundary resistance (R_{gb}) in the present LLZO thin film solid electrolyte #600-1.

The EIS measurements of the presented LLZO thin films are conducted with the in-plane test configuration shown in Fig. 6a. Their total ionic conductivities (σ_{total}) can be calculated according to the equation:

$$\sigma_{total} = \frac{L}{SR_{total}} \quad (1)$$

where L is the distance between the two contacting electrodes, S is the electrode area, and R_{total} is the total resistance of LLZO thin film determined through EIS measurements. The Nyquist plots of the measured impedance spectra (Fig. 6b and Figure S2a and S2b) are fitted with the equivalent circuit depicted in the inserts, which consists of a series combination of a constant phase element (CPE) with two circles of a resistor in parallel with a CPE. R_{bulk} and R_{gb} in the equivalent circuit represent the bulk resistance and the grain boundary resistance of the LLZO thin film. The grain boundary ionic conductivities (σ_{gb}) of LLZO thin films are also normalized to the distance of two parallel contacting electrodes, and can be calculated according to the following equation [39]:

$$\sigma_{gb} = \frac{L}{SR_{gb}} \frac{C_{bulk}}{C_{gb}} \quad (2)$$

where C_{bulk} and C_{gb} are the bulk capacitance and the grain boundary capacitance, which can be calculated using the equation (3) based on the fitted values of their

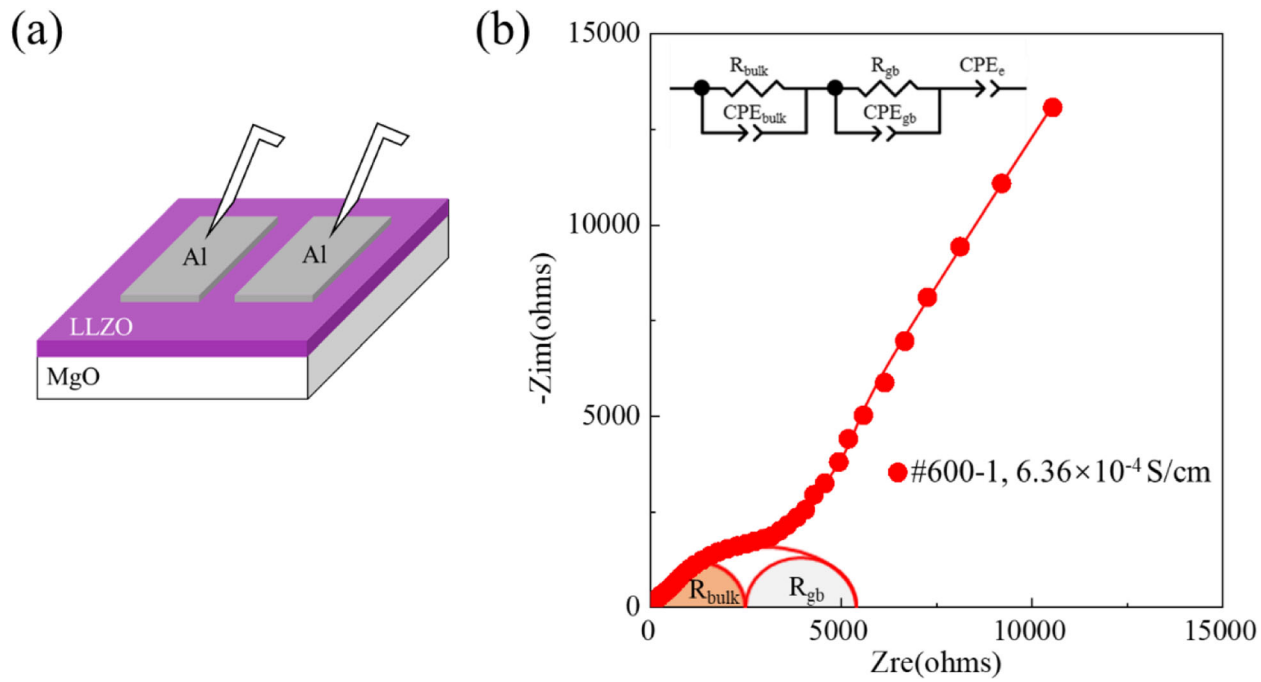

Fig. 6 **a** The in-plane test configuration for EIS measurements. **b** The Nyquist plot of impedance spectrum of LLZO thin film #600-1 measured at room temperature, insert shows the equivalent circuit for EIS analysis

corresponding R (R_{bulk} and R_{gb}) and CPE (CPE_{bulk} and CPE_{gb}) [34, 40].

$$C = \left(\mathrm{CPE} \times R^{1-n}\right)^{\frac{1}{n}} \quad (3)$$

The geometrical parameters (L and S) and the fitted values of the elements in the equivalent circuit (R_{total}, R_{bulk}, R_{gb}, C_{bulk}, and C_{gb}) are summarized in Table S2. Table 2 summarizes the calculated σ_{bulk}, σ_{gb}, and σ_{total} at room temperature of the presented LLZO thin films. σ_{total} of #800-1 is lower than 10^{-8} S/cm since it is dominated by the Li-poor phase of LZO. The samples with Ga dopant and extra Li, #800-2, #700-1, and #600-1, possess the σ_{total} of 5.63×10^{-7}, 3.89×10^{-5}, and 6.36×10^{-4} S/cm, respectively. This trend may be caused by two reasons. First, the proportion of high-resistive LZO in the prepared thin films is trimmed down as the annealing temperature is reduced, which is demonstrated by their XRD patterns (Fig. 3b–d). Second, the intensities of the diffraction peaks of #600-1 are much lower than that of the other two. Its low crystallinity may be related to the formation of amorphous domains between crystalline grains. As mentioned above, the amorphous domains between crystalline grains may lower the energy barrier for Li^+ transport across GBs (Fig. 1). In addition, the grain size of #600-1 is about 50 nm (Figure S3), which is smaller than the common values (hundreds of nanometers) reported in previous studies and may lead to a greater number of high-resistive GBs. However, the ionic conductivity of #600-1 reaches a cutting-edge value. These facts give a good indication that the strategy presented here to lower the energy barrier for Li^+ transport across GBs is effective. The analysis of EIS data indeed shows that σ_{gb} of #600-1 is closed to 2 orders of magnitude higher than that of #700-1, although it is difficult to quantify σ_{bulk} and σ_{gb} of #800-1 and #800-2 because of their high grain boundary resistance.

Table 2 Bulk ionic conductivities (σ_{bulk}), grain boundary ionic conductivities (σ_{gb}), and total ionic conductivities (σ_{total}) at room temperature of the presented LLZO thin films

Sample name	σ_{bulk} (S/cm)	σ_{gb} (S/cm)	σ_{total} (S/cm)
#800-1	/	/	7.86×10^{-9}
#800-2	/	/	5.63×10^{-7}
#700-1	1.03×10^{-4}	6.23×10^{-6}	3.89×10^{-5}
#600-1	1.33×10^{-3}	1.21×10^{-4}	6.36×10^{-4}

Conclusions

In summary, LLZO thin films with cubic phase and amorphous domains between crystalline grains were obtained through introducing Ga dopant and extra Li, and carefully optimizing annealing temperature. Firstly, the small energy disparity between Li^+ sites in the LLZO lattice of the cubic phase leads to a low energy barrier for Li^+ transport within crystalline grains. More importantly, the amorphous domains provide additional Li^+ vacant

sites around GBs and thus lower the energy barriers for Li^+ transport across GBs via relaxing the space charge effects. As a result, benefiting from the Li^+ transport paths with low migration energy barriers, the presented LLZO thin film exhibits an ionic conductivity of 6.36×10^{-4} S/cm at room temperature, which is attractive for applications in TFLBs.

Supplementary information

Supplementary information accompanies this paper at https://doi.org/10.1186/s11671-020-03378-x.

Additional file 1: Reduced energy barrier for Li^+ transport across grain boundaries with amorphous domains in LLZO thin-films. **Note S1:** The determination of thicknesses of each single layer of LLZO, Li_2CO_3, and Ga_2O_3. **Table S1.** The thickness of each single-layer thin film. **Table S2.** The geometrical parameters (L and S) of electrodes and the fitted values of the elements in the equivalent circuit (R_{total}, R_{bulk}, R_{gb}, C_{bulk}, and C_{gb}) of the different thin films for calculating σ_{total}, σ_{bulk}, and σ_{gb} at room temperature. **Figure S1.** The thickness of #600-1 (1.516 μm) determined in its cross-sectional SEM image. **Figure S2.** XRD patterns of the LLZO target used in this study. **Figure S3.** The grain size of #600-1(~50 nm) determined by SEM image. **Figure S4.** The Nyquist plots of impedance spectra of LLZO thin-films #700-1 (a), #800-1 (green in b), and #800-2 (brown in b) measured at room temperature, inserts show the equivalent circuits for EIS analysis.

Abbreviations

Li: Lithium; $Li_7La_3Zr_2O_{12}$ (LLZO): Lithium lanthanum zirconate; $La_2Zr_2O_7$ (LZO): Lanthanum zirconate; Li_2CO_3: Lithium carbonate; Ga_2O_3: Gallium(III) oxide; MgO: Magnesium Oxide; Ga: Gallium; La: Lanthanum; O: Oxygen; Zr: Zirconium; Al: Aluminum; Ta: Tantalum; Ar: Argon; Cu: Copper; TFLBs: Thin film lithium batteries; LiPON: Lithium phosphorus oxynitride; Li_2O: Lithium oxide; EB_g: Migration energy barrier for Li^+ transport within a grain; EB_{gb}: Migration energy barrier for Li^+ transport across the grain boundaries; GBs: Grain boundaries; σ_{total}: Total ionic conductivity; σ_{gb}: Grain boundary ionic conductivity; σ_{bulk}: Bulk ionic conductivity; C_{bulk}: Bulk capacitance; C_{gb}: Grain boundary capacitance; *R*: Resistor; CPE: Constant phase element; *L*: Distance between the two contacting electrodes; *S*: Electrode area; XRD: X-ray diffraction; TOF-SIMS: Time-of-flight secondary ion mass spectrometry; HRTEM: High-resolution transmission electron microscopy; EDX: Energy dispersive X-ray spectroscopy; EIS: Electrochemical impendence spectroscopy; AC: Alternating current

Acknowledgements

Not applicable.

Authors' Contributions

Yanlin Zhu, Xiaokun Zhang, Zongkai Yan, and Yong Xiang conceived and designed the experiments. Yanlin Zhu, Shuai Liu, and Zongkai Yan performed the experiments. Yanlin Zhu, Xiaokun Zhang, and Zongkai Yan analyzed the data. Yanlin Zhu, Yilan Pan, and Xiaokun Zhang wrote the paper. All authors read and approved the final manuscript.

Funding

This research work was financially supported by the National Science Funds of China (Grant No. 21905040), the Fundamental Research Funds for Central Universities (Contract No. ZYGX2019Z009), and the startup funds from the University of Electronic Science and Technology of China.

Availability of Data and Materials

The authors declare that the materials and data are promptly available to readers without undue qualifications for material transfer agreements. All data generated or analyzed during this study are included in this article.

Competing Interests

The authors declare that they have no competing interests.

Author details

[1]School of Materials and Energy, University of Electronic Science and Technology of China, Chengdu 611731, Sichuan, China. [2]Advanced Energy Research Institute, University of Electronic Science and Technology of China, Chengdu 611731, Sichuan, China.

Received: 23 May 2020 Accepted: 7 July 2020
Published online: 25 July 2020

References

1. Ostfeld AE, Gaikwad AM, Khan Y, Arias AC (2016) High-performance flexible energy storage and harvesting system for wearable electronics. Sci Rep 6: 26122
2. Janek J, Zeier WG (2016) A solid future for battery development. Nature Energy 1(9):1–4
3. García Núñez C, Manjakkal L, Dahiya R (2019) Energy autonomous electronic skin. npj Flexible Electronics 3(1):1–24
4. Chang J, Shang J, Sun Y, Ono LK, Wang D, Ma Z, Huang Q, Chen D, Liu G, Cui Y, Qi Y, Zheng Z (2018) Flexible and stable high-energy lithium-sulfur full batteries with only 100% oversized lithium. Nat Commun 9(1):4480
5. Li J, Ma C, Chi M, Liang C, Dudney NJ (2015) Solid electrolyte: the key for high-voltage lithium batteries. Adv Energy Materials 5(4):1401408
6. Teng S, Tan J, Tiwari A (2014) Recent developments in garnet based solid state electrolytes for thin film batteries. Curr Opinion Solid State Materials Sci 18(1):29–38
7. Albertus P, Babinec S, Litzelman S, Newman A (2017) Status and challenges in enabling the lithium metal electrode for high-energy and low-cost rechargeable batteries. Nature Energy 3(1):16–21
8. Gao Z, Sun H, Fu L, Ye F, Zhang Y, Luo W, Huang Y (2018) Promises, challenges, and recent progress of inorganic solid-state electrolytes for all-solid-state lithium batteries. Adv Mater 30(17):e1705702
9. Liu Q, Geng Z, Han C, Fu Y, Li S, He Y-b, Kang F, Li B (2018) Challenges and perspectives of garnet solid electrolytes for all solid-state lithium batteries. J Power Sources 389:120–134
10. Shoji M, Cheng EJ, Kimura T, Kanamura K (2019) Recent progress for all solid state battery using sulfide and oxide solid electrolytes. J Physics D 52(10): 103001
11. Pfenninger R, Struzik M, Garbayo I, Stilp E, Rupp JLM (2019) A low ride on processing temperature for fast lithium conduction in garnet solid-state battery films. Nature Energy 4(6):475–483
12. Rawlence M, Filippin AN, Wäckerlin A, Lin TY, Cuervo-Reyes E, Remhof A, Battaglia C, Rupp JLM, Buecheler S (2018) Effect of gallium substitution on lithium-ion conductivity and phase evolution in sputtered $Li_{7-3x}Ga_xLa_3Zr_2O_{12}$ thin films. ACS Applied Materials & Interfaces 10(16):13720–13728
13. Wang Y, Richards WD, Ong SP, Miara LJ, Kim JC, Mo Y, Ceder G (2015) Design principles for solid-state lithium superionic conductors. Nat Mater 14(10):1026–1031
14. Zhang X, Xie J, Shi F, Lin D, Liu Y, Liu W, Pei A, Gong Y, Wang H, Liu K, Xiang Y, Cui Y (2018) Vertically aligned and continuous nanoscale ceramic-polymer interfaces in composite solid polymer electrolytes for enhanced ionic conductivity. Nano Lett 18(6):3829–3838
15. Buschmann H, Dolle J, Berendts S, Kuhn A, Bottke P, Wilkening M, Heitjans P, Senyshyn A, Ehrenberg H, Lotnyk A, Duppel V, Kienle L, Janek J (2011) Structure and dynamics of the fast lithium ion conductor "$Li_7La_3Zr_2O_{12}$". Phys Chem Chem Phys 13(43):19378–19392
16. Wagner R, Redhammer GJ, Rettenwander D, Senyshyn A, Schmidt W, Wilkening M, Amthauer G (2016) Crystal structure of garnet-related Li-ion conductor $Li_{7-3x}Ga_xLa_3Zr_2O_{12}$: fast Li-ion conduction caused by a different cubic modification? Chemistry Materials 28(6):1861–1871
17. Bernstein N, Johannes MD, Hoang K (2012) Origin of the structural phase transition in $Li_7La_3Zr_2O_{12}$. Phys Rev Lett 109(20):205702
18. Dhivya L, Murugan R (2014) Effect of simultaneous substitution of Y and Ta on the stabilization of cubic phase, microstructure, and $Li(^+)$ conductivity of $Li_7La_3Zr_2O_{12}$ lithium garnet. ACS Appl Mater Interfaces 6(20):17606–17615
19. Yu S, Siegel DJ (2017) Grain boundary contributions to Li-ion transport in the solid electrolyte $Li_7La_3Zr_2O_{12}$ (LLZO). Chemistry of Materials 29(22):9639–9647
20. Shiiba H, Zettsu N, Yamashita M, Onodera H, Jalem R, Nakayama M, Teshima K (2018) Molecular dynamics studies on the lithium ion conduction behaviors depending on tilted grain boundaries with various symmetries in

garnet-type $Li_7La_3Zr_2O_{12}$. The Journal of Physical Chemistry C 122(38): 21755–21762
21. Xu X, Liu Y, Wang J, Isheim D, Dravid VP, Phatak C, Haile SM (2020) Variability and origins of grain boundary electric potential detected by electron holography and atom-probe tomography. Nat Mater 19:887–893
22. Xie H, Alonso JA, Li Y, Fernández-Díaz MT, Goodenough JB (2011) Lithium distribution in aluminum-free cubic $Li_7La_3Zr_2O_{12}$. Chemistry of Materials 23(16):3587–3589
23. Awaka J, Takashima A, Kataoka K, Kijima N, Idemoto Y, Akimoto J (2011) Crystal structure of fast lithium-ion-conducting cubic $Li_7La_3Zr_2O_{12}$. Chem. Lett. 40(1):60–62
24. Allen JL, Wolfenstine J, Rangasamy E, Sakamoto J (2012) Effect of substitution (Ta, Al, Ga) on the conductivity of $Li_7La_3Zr_2O_{12}$. J Power Sources 206:315–319
25. Chen Y-T, Jena A, Pang WK, Peterson VK, Sheu HS, Chang H, Liu R-S (2017) Voltammetric enhancement of Li-ion conduction in Al-doped $Li_{7-x}La_3Zr_2O_{12}$ solid electrolyte. J Phys Chem C 121(29):15565–15573
26. Ramakumar S, Deviannapoorani C, Dhivya L, Shankar LS, Murugan R (2017) Lithium garnets: synthesis, structure, Li^+ conductivity, Li^+ dynamics and applications. Progress Mater Sci 88:325–411
27. Jin Y, McGinn PJ (2011) Al-doped $Li_7La_3Zr_2O_{12}$ synthesized by a polymerized complex method. J Power Sources 196(20):8683–8687
28. Mukhopadhyay S, Thompson T, Sakamoto J, Huq A, Wolfenstine J, Allen JL, Bernstein N, Stewart DA, Johannes MD (2015) Structure and stoichiometry in supervalent doped $Li_7La_3Zr_2O_{12}$. Chem Mater 27(10):3658–3665
29. Qian X, Wang D, Zhang Y, Wu H, Pennycook SJ, Zheng L, Poudeu PFP, Zhao L-D (2020) Contrasting roles of small metallic elements M (M = Cu, Zn, Ni) in enhancing the thermoelectric performance of n-type $PbM_{0.01}Se$. J Mater Chem A 8(11):5699–5708
30. Rangasamy E, Wolfenstine J, Sakamoto J (2012) The role of Al and Li concentration on the formation of cubic garnet solid electrolyte of nominal composition $Li_7La_3Zr_2O_{12}$. Solid State Ionics 206:28–32
31. Shao C, Yu Z, Liu H, Zheng Z, Sun N, Diao C (2017) Enhanced ionic conductivity of titanium doped $Li_7La_3Zr_2O_{12}$ solid electrolyte. Electrochimica Acta 225:345–349
32. Thompson T, Wolfenstine J, Allen JL, Johannes M, Huq A, David IN, Sakamoto J (2014) Tetragonal vs. cubic phase stability in Al – free Ta doped Li7La3Zr2O12 (LLZO). J Mater Chem A 2(33):13431–13436
33. Wang D, Zhong G, Dolotko O, Li Y, McDonald MJ, Mi J, Fu R, Yang Y (2014) The synergistic effects of Al and Te on the structure and Li^+-mobility of garnet-type solid electrolytes. J Mater Chem A 2(47):20271–20279
34. Lobe S, Dellen C, Finsterbusch M, Gehrke HG, Sebold D, Tsai CL, Uhlenbruck S, Guillon O (2016) Radio frequency magnetron sputtering of $Li_7La_3Zr_2O_{12}$ thin films for solid-state batteries. J Power Sources 307:684–689
35. Sastre J, Tzu-Ying Lin TY, Filippin AN, Priebe A, Avancini E, Michler J, Tiwari AN, Romanyuk YE, Buecheler S (2019) Aluminum-assisted densification of cosputtered lithium garnet electrolyte films for solid-state batteries. ACS Appl. Energy Mater. 2:8511–8524
36. Garbayo I, Struzik M, Bowman WJ, Pfenninger R, Stilp E, Rupp JLM (2018) Glass-type polyamorphism in Li-garnet thin film solid state battery conductors. Adv Energy Mater 8(12):1702265
37. Zheng Z, Song S, Wang Y (2016) Sol-gel-processed amorphous lithium ion electrolyte thin films: structural evolution, theoretical considerations, and ion transport processes. Solid State Ionics 287:60–70
38. Huang Y, He Y, Sheng H, Lu X, Dong H, Samanta S, Dong H, Li X, Kim DY, Mao HK, Liu Y, Li H, Li H, Wang L (2019) Li-ion battery material under high pressure: amorphization and enhanced conductivity of $Li_4Ti_5O_{12}$. National Sci Rev 6(2):239–246
39. Wu JF, Guo X (2017) Origin of the low grain boundary conductivity in lithium ion conducting perovskites: $Li_{3x}La_{0.67-x}TiO_3$. Phys Chem Chem Phys 19(8):5880–5887
40. Loho C, Djenadic R, Mundt P, Clemens O, Hahn H (2017) On processing-structure-property relations and high ionic conductivity in garnet-type $Li_5La_3Ta_2O_{12}$ solid electrolyte thin films grown by CO_2 -laser assisted CVD. Solid State Ionics 313:32–44

Publisher's Note